STRUCTURAL BIOLOGY

ISSN 2059-7983

Depth-of-field extension in optical imaging for rapid crystal screening

Chen Li, Changqin Ding, Minghe Li, Jiayue Rong, Hilary Florian and Garth Simpson*

Department of Chemistry, Purdue University, 560 Oval Drive, West Lafayette, IN 47907, USA. *Correspondence e-mail: gsimpson@purdue.edu

Received 30 June 2020
Accepted 4 January 2021

Edited by M. Schiltz, Fonds National de la Recherche, Luxembourg

Keywords: depth-of-field extension; high throughput; crystal screening.

The depth of field (DoF) was extended 2.8-fold to achieve rapid crystal screening by retrofitting a custom-designed micro-retarder array (μRA) in the optical beam path of a nonlinear optical microscope. The merits of the proposed strategy for DoF enhancement were assessed in applications of second-harmonic generation imaging of protein crystals. It was found that DoF extension increased the number of crystals detected while simultaneously reducing the number of '*z*-slices' required for screening. Experimental measurements of the wavelength-dependence of the extended DoF were in excellent agreement with theoretical predictions. These results provide a simple and broadly applicable approach to increase the throughput of existing nonlinear optical imaging methods for protein crystal screening.

1. Introduction

Elucidation of macromolecular structures is a foundational step in understanding the biological functions of proteins. Facilitated by the development of synchrotron sources, conventional X-ray crystallography has contributed ∼89% of the protein structures recorded in the Protein Data Bank. Recent advances have seen ever higher throughput assays using ever-smaller volumes of solutions using emerging techniques such as serial femtosecond crystallography (SFX; Smith *et al.*, 2012), serial synchrotron crystallography (SSX; Meents *et al.*, 2017), microcrystal electron diffraction (MicroED; Clabbers *et al.*, 2017) *etc*. Serial X-ray crystallography using X-ray free-electron laser radiation (Martin-Garcia *et al.*, 2017) or synchrotron radiation has provided near-atomic resolution protein structures from microcrystals to nanocrystals (Boutet *et al.*, 2012). Meanwhile, MicroED has shown great potential as an alternative means for protein nanocrystallography (Clabbers *et al.*, 2017). However, limited access to XFEL/synchrotron facilities motivates in-house crystal optimization prior to different data collections. Therefore, high-throughput crystal-screening techniques to support the above-mentioned analyses are poised to enable further advances. A variety of fluorescence imaging techniques with submicrometre resolution and chemical specificities have been exploited to score protein crystals during the crystallization-condition screening process, such as UV fluorescence (Vernede *et al.*, 2006), intrinsic two-photon excited UV fluorescence (TPE-UVF; Madden *et al.*, 2011) and externally trace-labelled fluorescence (Groves *et al.*, 2007). Although widely applicable, all of the abovementioned techniques are still limited in crystalline

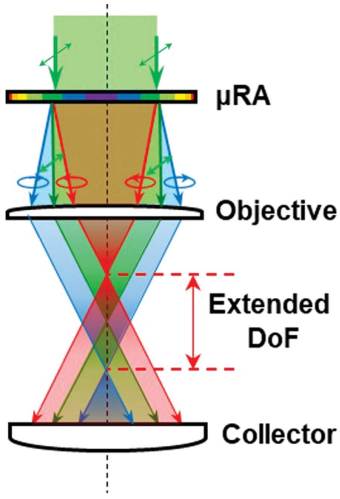

selectivity and sensitivity due to the nonzero background contributions from amorphous aggregates or solubilized fluorophores. Such sources of background are removed/suppressed by the symmetry selectivity in second-harmonic generation (SHG) and by the inherent confocal nature of multiphoton absorption in TPE-UVF.

SHG is a complementary imaging process that is highly selective for chiral crystals, including those of proteins. The symmetry requirements of SHG produce no coherent signal from disordered (solubilized or aggregated) proteins, but can often produce bright signals from protein crystals. By utilizing a femtosecond laser and beam-scanning apparatus, SHG microscopy allows selective optical screening of protein microcrystals (Haupert & Simpson, 2011), with bright SHG signal from individual protein crystals as small as ∼2 µm in diameter. In studies of integral membrane proteins in lipidic mesophases, SHG microscopy identified increases in hits of up to 40% relative to expert inspection of a panel of bright-field, cross-polarized, trace-labelled fluorescence and intrinsic fluorescence images (Kissick *et al.*, 2010). Using a correlation spectroscopy approach, SHG enabled detection of the presence of integral membrane-protein crystals of ∼100 nm in diameter for sample screening in femtosecond serial crystallography (Dow *et al.*, 2016). Furthermore, both SHG microscopy and TPE-UVF can be performed on a single instrument platform (Madden *et al.*, 2011). However, the tightly focused excitation beam typical in SHG and TPE-UVF imaging generally results in a relatively narrow depth of field (DoF) to the thickness of the mother liquor in a 96-well drop, often necessitating the acquisition of multiple '*z*-slices' through a well plate, increasing the overall measurement time.

Extending the DoF of an imaging system has been extensively investigated in order to increase the throughput of optical microscopic approaches. The simplest way to extend the DoF is to decrease the tightness of the focal spot by lowering the numerical aperture (NA) of excitation by using a narrow beam relative to the back aperture of the objective. However, NA reduction also increases the diameter of the point-spread function, which sacrifices resolution. More significantly, increasing the beam waist in the focal plane reduces the efficiency of both SHG and TPE-UVF, which scales quadratically with the incident intensity and approximately quartically with the NA. Other efforts are mostly based on wavefront-shaping approaches to elongate the axial point-spread function (PSF) of beams. Phase masks designed as an optical power apodizer have been reported to extend the DoF with the cost of ∼50% of power loss at the sample plane (Welford, 1960). Axicons have been deployed in a variety of nonlinear optical microscopes, including two-photon fluorescence microscopy (Dufour *et al.*, 2006) and stimulated Raman scattering microscopy (Chen *et al.*, 2017), to achieve an improved DoF by converting a Gaussian beam to a Bessel beam. Although such methods maximized the photon efficiency, retrofitting commercially available or pre-existing microscopes with an axicon pair is often nontrivial.

The present study reports an approach to extend the DoF of various optical imaging systems to 2.8-fold by the addition of a single one-inch optic to an existing optical microscope. By installing a laboratory-designed micro-retarder array (µRA) in the beam path, SHG images of a variety of crystalline samples were acquired in comparison with *z*-scanning images measured without the µRA. The extended DoF of an optical imaging system was both predicted theoretically and characterized via experimental measurements.

2. Experimental methods

$BaTiO_3$ nanocrystals (Sigma–Aldrich, 300 nm diameter) were immobilized in poly(ethylene glycol) (PEG; Sigma–Aldrich) with ∼1 mm thickness. The $BaTiO_3$ nanocrystals were first suspended in deionized water [∼1%(*w*/*w*)] and sonicated for 30 min prior to use. The PEG was mixed with 1 ml water [50%(*w*/*w*)] in a glass container and heated to melting (∼75°C) using a hotplate. After combining 100 µl with the $BaTiO_3$ suspension, the $BaTiO_3$–PEG mixture was sonicated for 1 min before spraying it onto a glass slide and cooling at room temperature until the PEG film solidified.

Ritonavir crystals were grown from seeded microcrystals sandwiched between ritonavir–copovidone amorphous solid dispersion (ASD) thin films prepared using a hydraulic press (Atlas Manual Hydraulic Press 15). To prepare the ASD films, 50–60 mg ASD powder was spread between two discs of aluminium foil placed in the film-making accessory with a 100 µm spacer. The chamber was heated to 115°C for 5 min and compressed at a pressure of four tons for 10 min. The temperature was then set to 65°C while keeping the pressure at four tons until the chamber was cooled to the setting point. The ritonavir–copovidone ASD films were removed from the press and cooled to room temperature. After the ritonavir microcrystals had been placed between two ASD films, a similar process was performed with a 250 µm spacer to make a crystal-seeded ritonavir–copovidone sandwich as detailed in Griffin *et al.* (2020). The prepared sandwich was kept at room temperature with controlled humidity for 48 h.

Tetragonal lysozyme crystals were prepared using a protocol adapted from Yaoi *et al.* (2004) and previously detailed in Newman *et al.* (2015). In brief, a 12.5 mg ml^{-1} solution of chicken egg-white lysozyme was prepared in nanopure water. Crystallization was achieved in 96-well plates by combining 1 µl protein solution with 1 µl NaCl–acetate buffer solution and keeping the wells sealed with tape overnight. Malachite green oxalate salt (Sigma–Aldrich) was dissolved in ethyl ethanoate (Sigma–Aldrich) to prepare a 500 µ*M* solution prior to use. Malachite green was introduced by adding 1 µl dye solution to 2 µl crystal mother liquor. The well was kept open for 10 min to allow the dye molecules to intercalate into the protein crystals and evaporate the ethyl ethanoate prior to SHG imaging.

The detailed design of the µRA has been described previously (Ding *et al.*, 2019). In brief, the µRA was designed to act as a 'chiral lens' with concentric patterns to induce half-wave retardance at every position varying spatially in the azimuthal orientation of the fast axis. The resulting pattern produced with linear incident polarization is identical to that

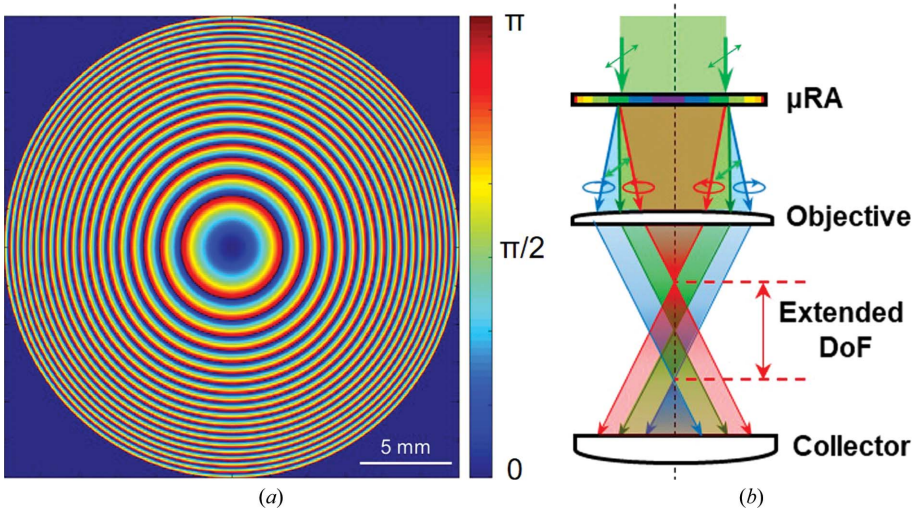

Figure 1
(*a*) The designed pattern of the μRA is shown as designed for half-wave retardance with varied azimuthal orientation of the fast axis (colour scale) targeted for 1064 nm light. (*b*) The working principle of the μRA is illustrated for generation of the extended DoF via polarization-wavefront shaping. The arrows indicate the polarization states of the incident light and the decomposed beamlets. Note: the use of different colours for the converging and diverging beamlets is for visualization only and is not meant to reflect wavelength-dependent dispersion effects.

produced by interference between diverging and converging orthogonal circular polarizations of light, such that the μRA operates as a concave lens for one circular polarization state and a convex lens for the other. The patterns were distributed quadratically on the one-inch optic, generating 22 concentric rings in total. The custom μRA was manufactured by Thorlabs Inc. by growing polymer liquid-crystal pixels on an N-BK7 glass substrate covered with antireflection coating targeting near-infrared wavelength. Characterizations of the μRA and the extension ratio of the DoF were performed on a laboratory-built beam-scanning SHG microscope. Beam scanning was performed with a resonant vibrating mirror (∼8 kHz; EOPC) along the fast-axis scan and a galvanometer (Cambridge Technology) for slow-axis scanning. The incident beam was provided by a Mai Tai 80 MHz Ti:sapphire pulsed laser (Spectra Physics) with 100 fs pulses. The beam was focused on the sample with both a 10× objective with a working distance of 16 mm (Nikon; NA = 0.30) and a 20× objective with a working distance of 6 mm (Nikon; NA = 0.45). The incident wavelength was tuneable within the range 750–1000 nm, with an average power of 50 mW at the sample plane. Each SHG image was obtained by signal averaging four sequential raw images with a total acquisition time of 250 ms. SHG signal was collected with a KG-3 infrared absorbing filter and a shortpass filter (cutoff wavelength of 600 nm) placed before the photomultiplier tube detector (PMT) to remove the fundamental light. *MATLAB* code was written in-house to control the scanning mirrors and communication with the data-acquisition electronics. When integrating the μRA, the incident laser power was typically increased (doubled) to maintain similar intensity within each focal plane.

To evaluate applications in automated crystal screening, SHG images of $BaTiO_3$ nanocrystals, ritonavir crystals and lysozyme crystals intercalated with the SHG contrast agent malachite green (Newman *et al.*, 2015) were acquired on a commercial second-harmonic generation microscope capable of supporting high-throughput chiral crystal screening (SONICC, Formulatrix). *ImageJ* was used to analyse and produce all SHG images (Schneider *et al.*, 2012).

3. Results and discussion

A simulated pattern of the μRA and a schematic of DoF extension in imaging systems are shown in Fig. 1. The μRA used in this work was designed with a liquid-crystal film producing half-wave retardance of 1064 nm light at every pixel with the fast-axis angle rotated radially, which has qualitative similarities to a Fresnel zone plate (FZP), as shown in Fig. 1(*a*). The coherent combination of right and left circularly polarized beams of equal amplitude produces linearly polarized light, the axis of polarization of which is dictated by the phase shift between the two circular polarizations. As such, the particular pattern of linearly polarized light programmed to be produced by the μRA is identical to that expected from the interference between a pair of slightly converging and slightly diverging circularly polarized beams of orthogonal polarization. Once this pattern for the spatially varying polarization has been produced by the μRA, the wavefront will simply propagate as if produced by the coherent combination of the two orthogonally polarized beamlets. The azimuthal angle (θ) as a function of position coordinates (x, y) on the μRA on a per-pixel basis is described as $\theta(x, y) = 2\pi[(x - R)^2 + (y - R)^2]/4\lambda f$, where R is the active radius of the μRA, λ is the design wavelength (in this case 1064 nm) and f is the focal length, designed to be 6.28 m with a 1064 nm incident beam. As in the schematic in Fig. 1(*b*), an objective lens focuses all beamlets at different focal planes, resulting in an extended DoF compared with that of a conventional imaging system.

To assess the practical performance of the extended DoF for crystal screening with improved throughput, SHG images of $BaTiO_3$ nanoparticles were collected as a proof of concept using an SHG microscope with and without the μRA installed. As shown in Figs. 2(*a*)–2(*d*), a series of SHG images acquired at four different z-axis positions represent a typical crystal-screening process, recognizing $BaTiO_3$ crystals located in multiple focal planes. Fig. 2(*e*) is the z-projection of Figs. 2(*a*)–2(*d*) and exhibits the intact information of all crystals distributed within the 160 μm z-scanning range. Fig. 2(*f*) is a single SHG image of the same field of view obtained with the μRA in the system. A side-by-side comparison of Figs. 2(*e*) and 2(*f*) shows that all of the crystals that appeared in the z-projection of four SHG images were registered in the snapshot with the μRA, indicating that the data-acquisition

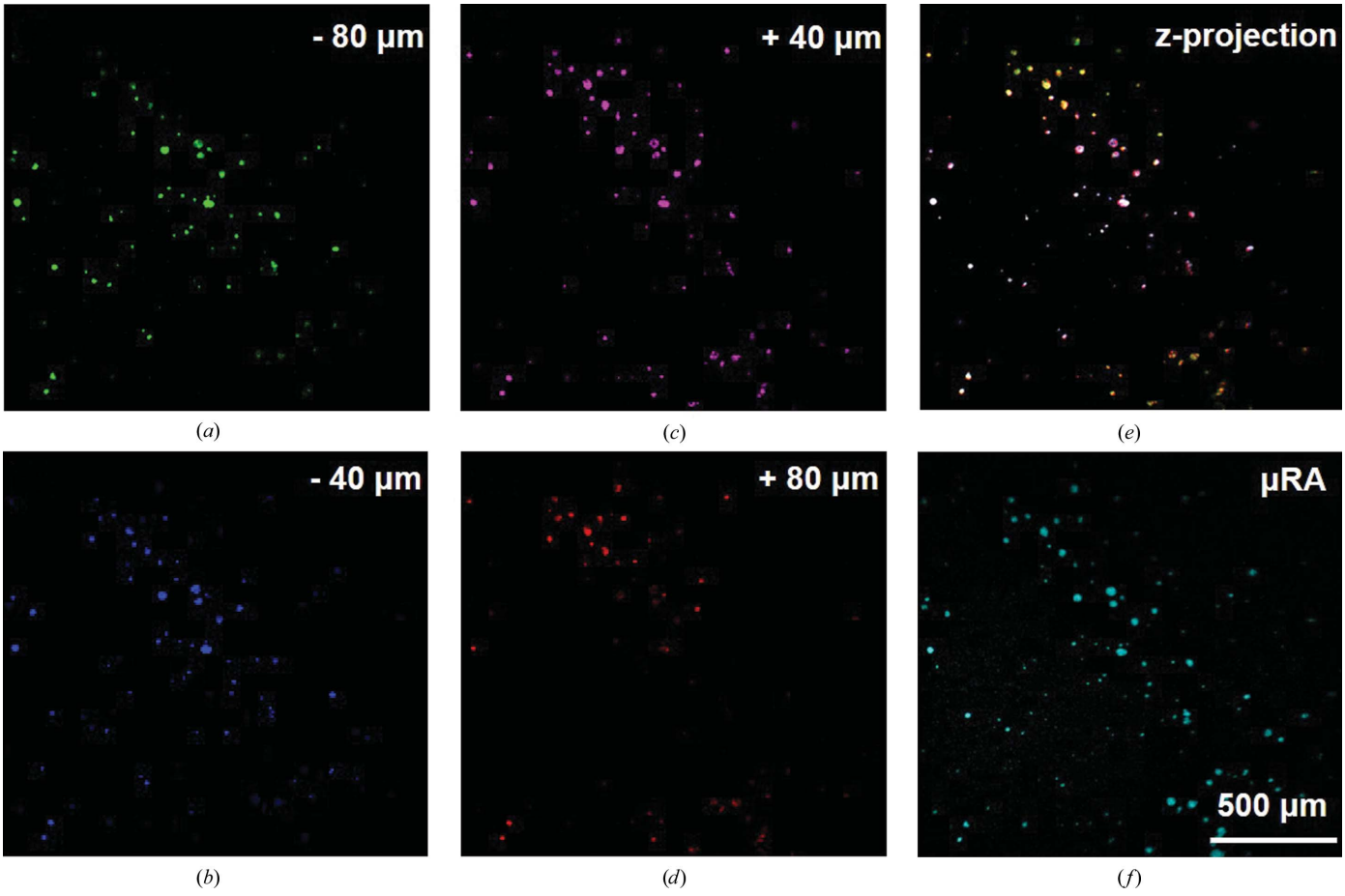

Figure 2
(*a*)–(*d*) SHG images of $BaTiO_3$ nanoparticles measured at different *z*-axis positions. (*e*) *z*-projection of (*a*)–(*d*). (*f*) Single SHG image of the same field of view with the µRA.

time could be reduced by a factor of approximately three in a practical crystal-screening process. For samples with a thicknesses greater than the enhanced depth of field, integration of the chiral lens could enable an approximately threefold increase in step size in *z*-scanning (with corresponding time reductions) without a loss of crystal coverage.

The presented chiral lens approach was also investigated using ritonavir crystals grown in copovidone in comparison with *z*-scanning SHG imaging. The *z*-projection of multiple SHG images collected at different *z*-axis positions and the single SHG image of the same field of view with extended DoF are shown in Figs. 3(*a*) and 3(*b*), respectively. To better compare the detected crystals in both methods, a colour-threshold overlay of the two images is shown in Fig. 3(*c*), in which most pixels are yellow, representing crystals that were detected in both Figs. 3(*a*) and 3(*b*). The violet pixels in Fig. 3(*c*) correspond to ritonavir crystal positions detected only in the image measured with the µRA installed in the microscope (Fig. 3*b*). A Venn diagram indicating the pixels detected by *z*-scanning versus single-shot measurement with the chiral lens installed is shown in Fig. 3(*d*). The preferential detection of a greater fraction of crystals with the chiral lens installed is tentatively attributed to the minimization of the measurement bias associated with the dependence of the SHG signal intensity on crystal azimuthal orientation (Takebayashi *et al.*, 1997). Since linearly polarized excitation light was used in the measurement of Fig. 3(*a*), those rod-like ritonavir crystals with long axes perpendicular to the polarization orientation produced noticeably less SHG signal. However, the majority of the excitation light was circularly polarized with the deployment of the µRA in the measurement of Fig. 3(*b*), which exhibited more uniform SHG intensity for randomly oriented ritonavir crystals compared with Fig. 3(*a*). The comparatively small fraction of pixels preferentially detected by *z*-scanning is tentatively attributed to the image blurring associated with integration over both in-focus and out-of-focus *z*-planes, which is consistent with the green pixels generally appearing as halos around crystals mutually identified by both methods. Evaluated over seven unique fields of view converted to binary form (*i.e.* background = 0, crystal = 1), single-shot measurements using the chiral lens resulted in a consistent increase in the number of detected pixels attributed to crystals when compared with integration over multiple *z*-scan measurements (after optimizing alignment by cross-correlation).

To further demonstrate the utility of the presented approach in macromolecule crystal screening, SHG images of tetragonal lysozyme crystals intercalated with malachite green

molecules were acquired and are summarized in Fig. 4. Figs. 4(*a*), 4(*b*) and 4(*c*) show three SHG images obtained at different *z*-axis positions covering 300 µm via the conventional approach. The *z*-projection of all three images is shown in Fig. 4(*d*). In comparison, an SHG image of the same field of view collected with the extended DoF is shown in Fig. 4(*e*). It can be seen that all of the crystals detected in Fig. 4(*d*) were observed in Fig. 4(*e*). In addition, the yellow and red circles selected several crystals that are dim in the conventional SHG image but bright in the extended DoF measurements attributed to the azimuthal dependence of SHG signals discussed in the preceding section.

The change in depth of field introduced by addition of the µRA chiral lens was measured using a knife-edge approach, the results of which are summarized in Fig. 5. In the figure, the axial beam profile of an imaging system with a 20× objective lens was measured with and without the µRA installed in the beam path. To recover the beam profile in the *xz* plane (Figs. 5*a* and 5*b*), sharp-edge image analysis was performed on a stack of *z*-scanning bright-field images of a razorblade placed near the centre of the beam focus, in which the derivative of the intensity profile along an edge was fitted to a Gaussian function to retrieve the r.m.s. (root-mean-squared) beam width. It is noteworthy that the beam width at the focus remained unchanged following installation of the µRA, which is consistent with the lack of detectable loss in the spatial resolution of the microscope with this approach. The PSFs of the system measured under both imaging conditions are plotted in Fig. 5(*c*), indicating an extension ratio of ∼2.8 by comparing the FWHM (full-width at half-maximum) of the original DoF (black) with the extended DoF (red).

For different wavelength sources, the DoF can be designed to controllably distribute power over two or three foci. Knowledge of geometrical optics describing Fresnel zone plate and thin lenses were deployed to predict the extended DoF with the µRA as a function of incident-light wavelength in an imaging system. For instance, the µRA serves as a positive FZP for the converging left circular polarization (LP) component, the focal length of which is expressed as (Cao & Jahns, 2004)

$$f_{\mu\mathrm{RA}} = \frac{R_n^2}{n \cdot \lambda} - \frac{n \cdot \lambda}{4} \simeq \frac{R_n^2}{n \cdot \lambda}, \qquad (1)$$

where R_n is the radius of the nth zone of the zone plate. For the µRA used in this work, n = 22 and R_n = 12.5 mm. In contrast, the µRA serves as a negative FZP for the diverging

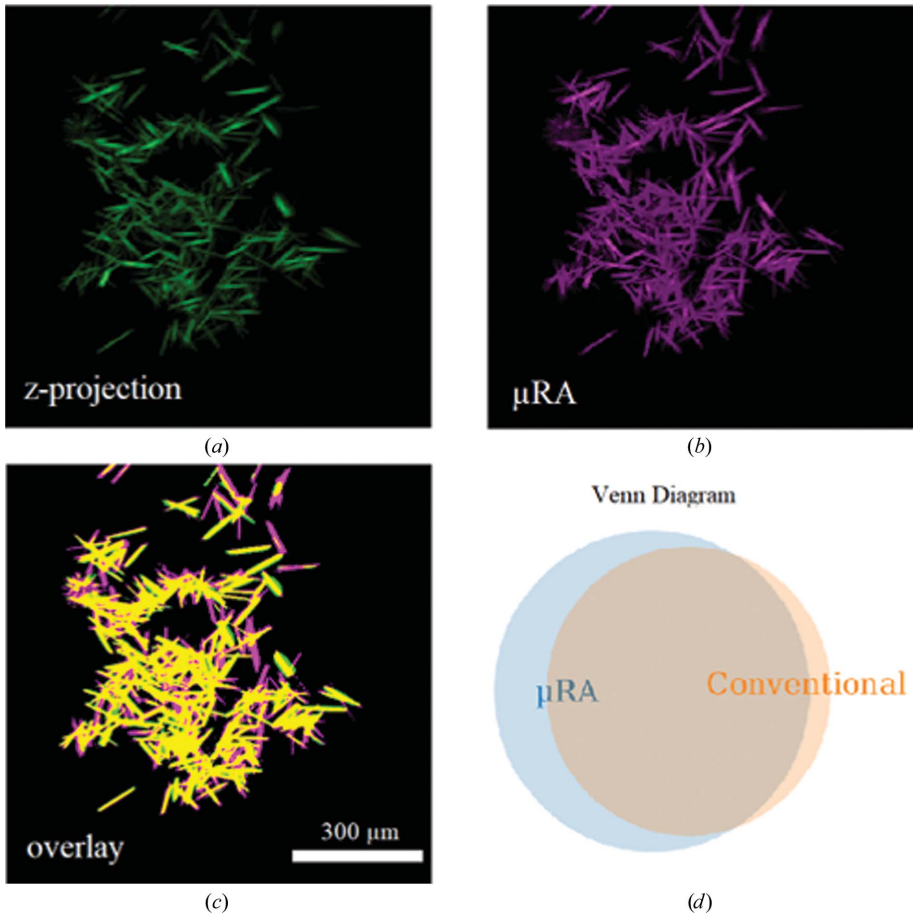

Figure 3
(*a*) Integrated intensity from a series of SHG images of ritonavir crystals measured by *z*-scanning. (*b*) Single-shot SHG image of the same field of view with the µRA. (*c*) A colour overlay of binary images of (*a*) and (*b*). (*d*) Venn diagram showing the fraction of crystals detected with the µRA and with *z*-scanning.

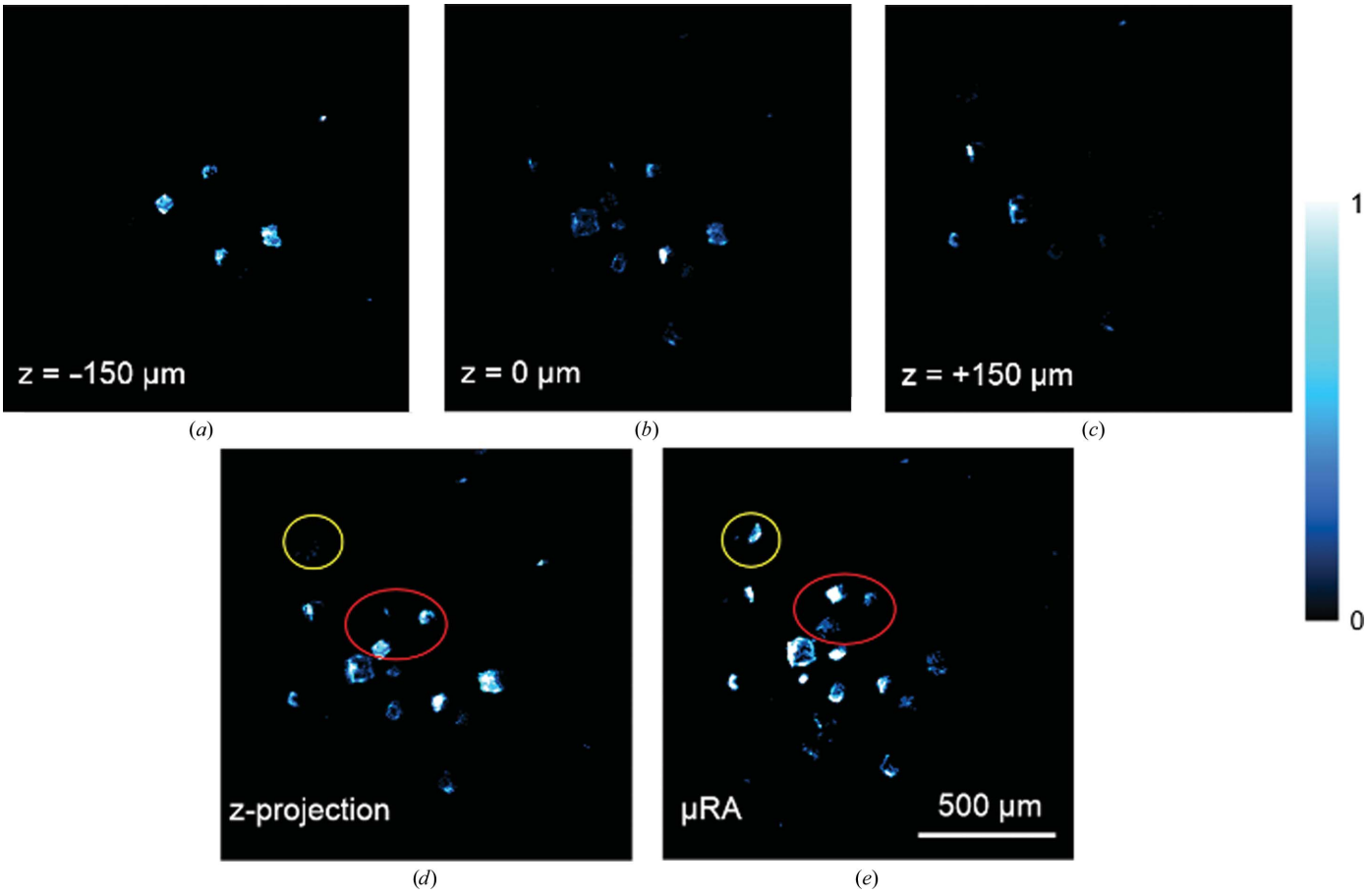

Figure 4
(*a*)–(*c*) SHG images of lysozyme crystals intercalated with malachite green at various *z*-axis positions. (*d*) *z*-projection of (*a*)–(*c*). (*e*) SHG image of the same field of view with the µRA using the same exposure time.

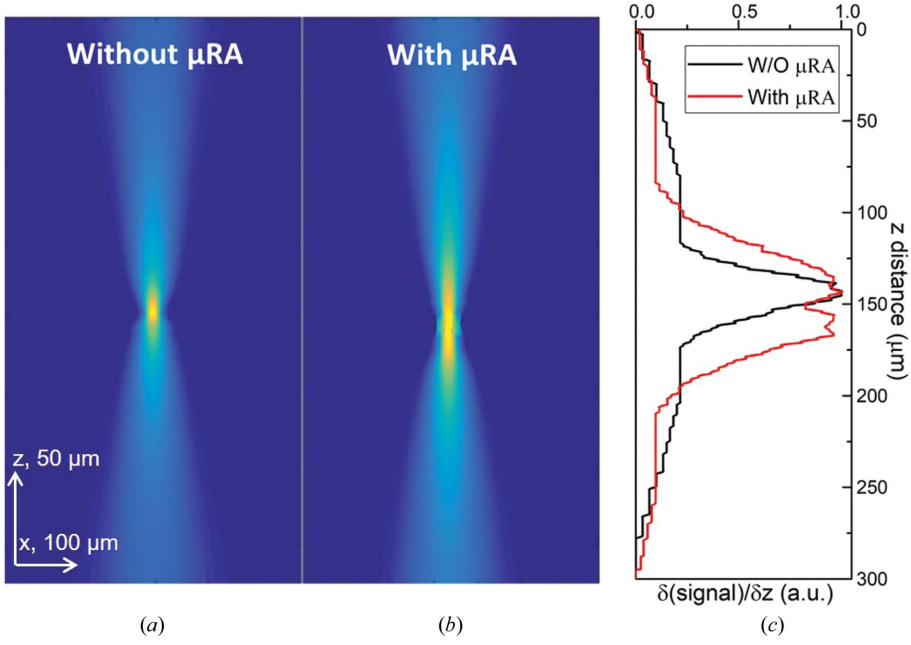

Figure 5
The measured point-spread functions in the *xz* plane before (*a*) and after (*b*) the installation of the µRA in the optical beam path. (*c*) The point-spread functions along the *z*-axis with and without the µRA yielded a measured extension ratio of the DoF of 2.8 for a 20× objective.

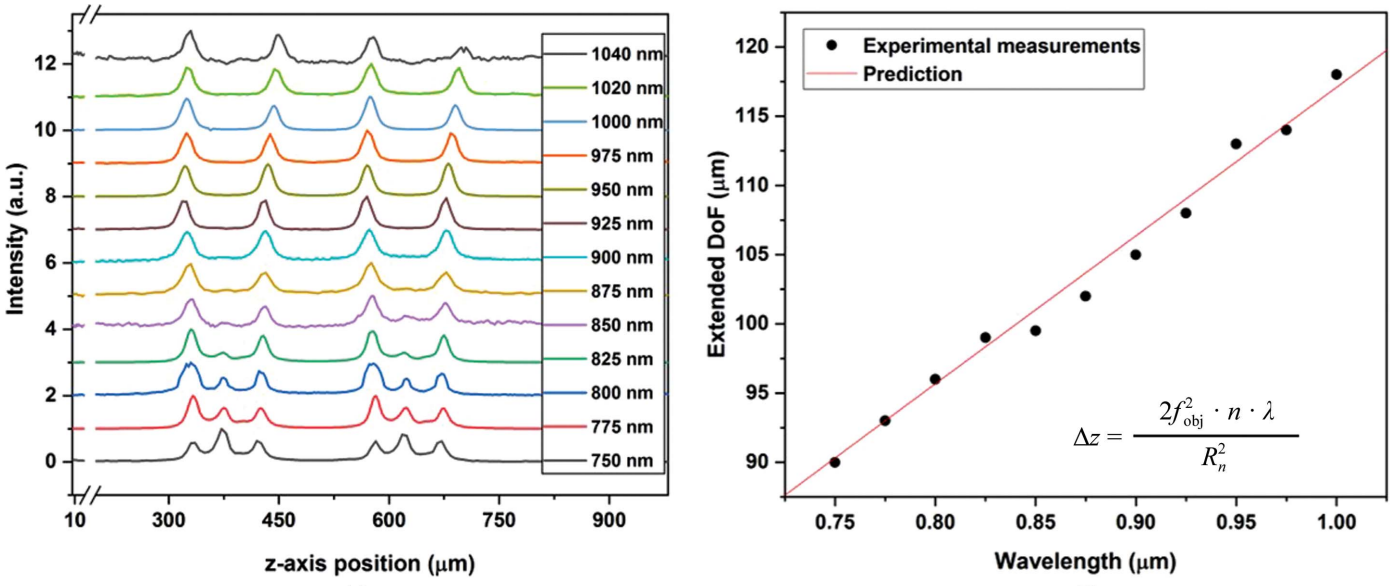

(*a*) (*b*)

Figure 6
(*a*) Depth-resolved SHG intensity of *z*-cut quartz measured with extended DoF and varied excitation wavelength. (*b*) Comparison of theoretical prediction (red line) and measurements (plots) of the extended DoF as a function of the excitation wavelength.

RP light with a focal length of $-f_{\mu RA}$. Thus, the combination of the μRA and an objective lens were considered as either a convex–convex system (the converging LP component) or a concave–convex system (the diverging RP component). Denoting the focal length of the objective lens as f_{obj}, the equivalent focal lengths are described by the following equations with the thin-lens approximation, respectively:

$$f_{LP} = \frac{f_{obj} f_{\mu RA}}{f_{\mu RA} + f_{obj}}, \tag{2}$$

$$f_{RP} = \frac{f_{obj} f_{\mu RA}}{f_{\mu RA} - f_{obj}}. \tag{3}$$

The distance between the LP and RP foci is defined as the extended DoF, shown as

$$\mathrm{DoF}_{extended} = f_{RCP} - f_{LCP} = \frac{2f_{obj}^2 f_{\mu RA}}{f_{\mu RA}^2 - f_{obj}^2} \tag{4}$$

Given the fact that $f_{\mu RA} \gg f_{obj}$ in a typical microscope, (4) can be rewritten as

$$\mathrm{DoF}_{extended} \cong \frac{2f_{obj}^2}{f_{\mu RA}}. \tag{5}$$

After substituting (1) into (5), the relationship between the extended DoF and the incident beam wavelength is expressed as

$$\mathrm{DoF}_{extended} = \frac{2f_{obj}^2 \cdot n}{R_n^2} \cdot \lambda. \tag{6}$$

In brief, the wavelength-dependence of the extended DoF is determined mainly by the focal length of the objective lens for a determined μRA.

To assess the validity of the theoretical prediction in (6), *z*-scanning SHG images of *z*-cut quartz with different excitation wavelengths were acquired using a 10× objective (f_{obj} = 19.5 mm). The integrated SHG intensity at each *z*-axis position with varying excitation wavelength is summarized in Fig. 6(*a*). Each peak in the SHG intensity trace indicates that one surface of the *z*-cut quartz was placed at one of the axially offset foci. If the μRA were designed with perfect half-wave retardance (Γ = λ/2, in which λ is the incident wavelength), it would serve as a 'chiral lens', in which the right and left circularly polarized components of light emerging from the μRA would produce a pair of axially offset foci following passage through the objective. By detuning the retardance of the μRA away from half-wavelength (Γ > λ/2), a third residual 'zero-order' beam appears in the original focal plane, the relative intensity of which can be tuned by appropriate design of the μRA. When using a μRA designed for half-wave retardance at 1064 nm, the laser power distributed to the middle focus decreases as the incident wavelength approaches the design wavelength. Therefore, six peaks were observed in traces with shorter excitation wavelengths, while only four peaks were seen when it was tuned to above 850 nm. The separation distances at various excitation wavelengths between the side peaks (top LP plane and bottom RP plane) were plotted in comparison with the predicted extended DoF (red line) from (6) as shown in Fig. 6(*b*). The predicted unitless slope of 107 was in excellent agreement with the experimental slope of 108.

4. Conclusion

The use of a laboratory-designed μRA to extend the DoF of optical microscopy has been demonstrated for rapid crystal screening. With the addition of the μRA to an existing imaging

system, the DoF was shown to increase to 2.8-fold while concurrently increasing the total number of crystalline pixels detected. The increased coverage is tentatively attributed to the generation of circularly polarized light in the two offset foci, reducing bias in the SHG intensity from the crystal orientation. Experimental measurements of the wavelength-dependence of the extended DoF were in excellent agreement with theoretical predictions. SHG images of $BaTiO_3$ nanoparticles, ritonavir crystals and malachite green-intercalated protein crystals were acquired to validate the universality of the presented approach in the detection of salts, small molecules and macromolecules. Integration of the chiral lens into the beampath of a commercial SONICC instrument required only straightforward modification of the removable objective assembly. Finally, the simplicity of experimental implementation presents opportunities for extension to many other optical imaging techniques for protein crystal screening (for example, bright-field imaging, UV fluorescence and TPE-UV), as well as applications beyond crystal screening.

Funding information

The authors gratefully acknowledge support from the National Institutes of Health (R01GM-103401). CL would also like to acknowledge financial support from Purdue Research Foundation and the Dr Ching Siang Yeh Fellowship.

References

Boutet, S., Lomb, L., Williams, G. J., Barends, T. R. M., Aquila, A., Doak, R. B., Weierstall, U., DePonte, D. P., Steinbrener, J., Shoeman, R. L., Messerschmidt, M., Barty, A., White, T. A., Kassemeyer, S., Kirian, R. A., Seibert, M. M., Montanez, P. A., Kenney, C., Herbst, R., Hart, P., Pines, J., Haller, G., Gruner, S. M., Philipp, H. T., Tate, M. W., Hromalik, M., Koerner, L. J., van Bakel, N., Morse, J., Ghonsalves, W., Arnlund, D., Bogan, M. J., Caleman, C., Fromme, R., Hampton, C. Y., Hunter, M. S., Johansson, L. C., Katona, G., Kupitz, C., Liang, M., Martin, A. V., Nass, K., Redecke, L., Stellato, F., Timneanu, N., Wang, D., Zatsepin, N. A., Schafer, D., Defever, J., Neutze, R., Fromme, P., Spence, J. C. H., Chapman, H. N. & Schlichting, I. (2012). *Science*, **337**, 362–364.

Cao, Q. & Jahns, J. (2004). *J. Opt. Soc. Am. A*, **21**, 561–571.

Chen, X., Zhang, C., Lin, P., Huang, K.-C., Liang, J., Tian, J. & Cheng, J.-X. (2017). *Nat. Commun.* **8**, 15117.

Clabbers, M. T. B., van Genderen, E., Wan, W., Wiegers, E. L., Gruene, T. & Abrahams, J. P. (2017). *Acta Cryst.* D**73**, 738–748.

Ding, C., Li, C., Deng, F. & Simpson, G. J. (2019). *Opt. Express*, **27**, 3837–3850.

Dow, X. Y., Dettmar, C. M., DeWalt, E. L., Newman, J. A., Dow, A. R., Roy-Chowdhury, S., Coe, J. D., Kupitz, C., Fromme, P. & Simpson, G. J. (2016). *Acta Cryst.* D**72**, 849–859.

Dufour, P., Piché, M., De Koninck, Y. & McCarthy, N. (2006). *Appl. Opt.* **45**, 9246–9252.

Griffin, S. R., Takanti, N., Sarkar, S., Song, Z., Vogt, A. D., Danzer, G. D. & Simpson, G. J. (2020). *Mol. Pharm.* **17**, 4564–4571.

Groves, M. R., Müller, I. B., Kreplin, X. & Müller-Dieckmann, J. (2007). *Acta Cryst.* D**63**, 526–535.

Haupert, L. M. & Simpson, G. J. (2011). *Methods*, **55**, 379–386.

Kissick, D. J., Gualtieri, E. J., Simpson, G. J. & Cherezov, V. (2010). *Anal. Chem.* **82**, 491–497.

Madden, J. T., DeWalt, E. L. & Simpson, G. J. (2011). *Acta Cryst.* D**67**, 839–846.

Martin-Garcia, J. M., Conrad, C. E., Nelson, G., Stander, N., Zatsepin, N. A., Zook, J., Zhu, L., Geiger, J., Chun, E., Kissick, D., Hilgart, M. C., Ogata, C., Ishchenko, A., Nagaratnam, N., Roy-Chowdhury, S., Coe, J., Subramanian, G., Schaffer, A., James, D., Ketwala, G., Venugopalan, N., Xu, S., Corcoran, S., Ferguson, D., Weierstall, U., Spence, J. C. H., Cherezov, V., Fromme, P., Fischetti, R. F. & Liu, W. (2017). *IUCrJ*, **4**, 439–454.

Meents, A., Wiedorn, M. O., Srajer, V., Henning, R., Sarrou, I., Bergtholdt, J., Barthelmess, M., Reinke, P. Y. A., Dierksmeyer, D., Tolstikova, A., Schaible, S., Messerschmidt, M., Ogata, C. M., Kissick, D. J., Taft, M. H., Manstein, D. J., Lieske, J., Oberthuer, D., Fischetti, R. F. & Chapman, H. N. (2017). *Nat. Commun.* **8**, 1281.

Newman, J. A., Scarborough, N. M., Pogranichniy, N. R., Shrestha, R. K., Closser, R. G., Das, C. & Simpson, G. J. (2015). *Acta Cryst.* D**71**, 1471–1477.

Schneider, C. A., Rasband, W. S. & Eliceiri, K. W. (2012). *Nat. Methods*, **9**, 671–675.

Smith, J. L., Fischetti, R. F. & Yamamoto, M. (2012). *Curr. Opin. Struct. Biol.* **22**, 602–612.

Takebayashi, M., Mizutani, G. & Ushioda, S. (1997). *Opt. Commun.* **133**, 116–122.

Vernede, X., Lavault, B., Ohana, J., Nurizzo, D., Joly, J., Jacquamet, L., Felisaz, F., Cipriani, F. & Bourgeois, D. (2006). *Acta Cryst.* D**62**, 253–261.

Welford, W. T. (1960). *J. Opt. Soc. Am.* **50**, 749–753.

Yaoi, M., Adachi, H., Takano, K., Matsumura, H., Inoue, T., Mori, Y. & Sasaki, T. (2004). *Jpn. J. Appl. Phys.* **43**, L1318–L1319.